Research Article

Journal of Environmental Nanotechnology

Enhanced Electrochemical and Dielectric Properties of rGO–TiO_2 Modified PTh/PEO Nanofibers Synthesized by Electrospinning

S. Sandip Khedkar[1], S. Karthick[2], A. Rajkumar[3], B. Gayathri[4*] and Nestor Ulloa[5]

[1]Department of Mechanical Engineering, Yeshwantrao Chavan College of Engineering, Hingana Road, Wanadongri, Nagpur, MH, India
[2]Department of Mechanical Engineering, JJ college of engineering and technology, Tiruchirapalli, TN, India
[3]Department of Mechanical Engineering, Rajalakshmi Engineering College, Thandalam, Chennai, TN, India
[4]Department of Computer Science, Bishop Heber College (Autonomous), Trichy, TN, India
[5]Department of Mechanical Engineering, Escuela Superior Politécnica de Chimborazo (ESPOCH), Riobamba, Ecuador
Received: 27.11.2025 Accepted: 09.02.2026 Published: 30.03.2026
*bgayathri.7890@gmail.com

ABSTRACT

Influence of reduced graphene oxide (rGO) and nanoparticles (NPs) of titanium dioxide (TiO_2) as additions on polythiophene (PTh)/polyethylene oxide (PEO) nanofibers has been investigated in this study by employing an electrospinner. The alternate electrical conductance and dielectric characteristics were assessed as functions of temperature (30 – 100 °C) and frequency (1 – 200 kHz) for PTh/PEO/rGO/xTiO_2 (x = 0, 0.0015, 0.003, 0.0045, 0.006) nanofiber. Dielectric properties show TiO_2 NPs improved both the conductivity and dielectric constant, while simultaneously decreasing dielectric loss. The electrochemical performance was evaluated by cyclic voltammetry, galvanostatic charge-discharge, and electrochemical impedance spectroscopy in a 1 M KOH solution. The improved composite demonstrated an areal capacitance of 408.35 mF cm^{-2} and maintained 93.06% capacitance after 10,000 cycles. The enhanced performance is ascribed to the synergistic interaction between rGO and TiO_2 nanoparticles, which facilitate charge transfer and electrolyte diffusion. The results suggest that PTh/PEO/rGO/TiO_2 nanofibers are viable materials for supercapacitor electrodes and dielectric applications.

Keywords: Reduced graphene oxide; Electrospinning; Titanium dioxide; Polyethylene oxide; Electrochemical test; Dielectric constant.

1. INTRODUCTION

Conducting polymer nanocomposites are promising materials for energy storage and dielectric applications due to their tunable electrical properties. The enhancement in dielectric behavior is primarily governed by interfacial polarization arising from the heterogeneous interfaces between the polymer matrix (PTh/PEO) and the embedded rGO and TiO_2 nanoparticles. Under an applied electric field, charge carriers accumulate at these interfaces due to differences in conductivity and permittivity. Therefore, interfacial polarization not only enhances dielectric properties but also plays a crucial role in nanofiber formation and morphology control. Electrospun PTh/PEO/rGO/TiO_2 nanofibers therefore offer enhanced electrochemical and dielectric performance suitable for supercapacitor and advanced electronic applications. A flexible solid polymer electrolyte (SPE), Ca at SA/ZIF-8-PEO was fabricated by electrospinning for solid-state sodium-ion batteries. The synergy of ZIF-8 and Ca^{2+}-crosslinked sodium alginate (SA) reduced PEO crystallinity, improved Na^+ migration number (0.45) and Na^+ (4.4×10^{-4} S cm^{-1}). The Na/Ca@SA/ZIF-8-PEO/Na cell achieved ~1500 h stability and 92 mAh g^{-1} after 1000 cycles (Hong *et al.* 2026). Mn- and Li-doped calcium phosphates were incorporated into chitosan (CS)/polyethylene oxide (PEO) electrospun nanofibers (NFs) for cancer therapy. The CPs showed strong ROS and H_2O_2 generation with selective cytotoxicity on A375 melanoma cells. MTT, Annexin V/PI, and qPCR assays revealed upregulation of P53, Bax and apoptosis enhancement (Gorgani *et al.* 2025). A self-standing Si//PCNF-15 anode was developed by embedding silicon nanoparticles (Si/NPs) uniformly in carbon nanofibers (CNF) using Pluronic P123 as dispersant. The electrode showed capacity rate of 236.1 mAh g^{-1} (10 A g^{-1}) and specific capacity of 1074.8 mAh g^{-1} (0.3 A g^{-1}). The approach enables homogeneous Si–CNF composite fabrication for lithium-ion batteries (LIBs) (Wang *et al.* 2023a). A 3D ZIF-8 network-reinforced PEO composite electrolyte was built by assembling ZIF-8 on carboxylated NFs. The interpenetrated MOF network improved Li^+ conductivity (4.39×10^{-4} S cm^{-1}), Li^+ transference number (0.42), and

stability (~4.9 V). $LiFePO_4$/Z-C-PAN-PEO/Li cells delivered 116.2 mAh g^{-1} after 600 cycles, showing excellent dendrite suppression (Wang *et al.* 2023b).

A polymeric ionic liquid was formed by grafting methyl methacrylate and vinyl imidazolium iodide (VIMI) onto PEO, followed by inserting WO_3 nanoparticles to generate PVIM-W nanofibers by electrospinning. An electrolyte was used in quasi-solid-state dye and sensitized solar cells (QSS-DSSC); it achieved 7.2% efficiency and retained 94.4% stability after 500 h. The SEM revealed uniform, beadless fibers supporting improved photovoltaic performance over liquid electrolytes (Thomas and Rajiv, 2020). Parallel electrospinning produced PVP/$Ti(SO_4)_2$ and PVP/$SnCl_4$ Janus NFs, which after calcination formed TiO_2//SnO_2 Janus NFs for gas sensing. The MOS-based sensor exhibited fast response–recovery and high ethanol selectivity. The Janus structure improved charge transport and surface reaction, demonstrating a design pathway for high-performance TiO_2–SnO_2 gas sensors (Li *et al.* 2020). Electrospun TiO_2 nanofibers embedded with $BaTiO_3$ (BTO@TO_nfs) were incorporated into P(VDF-TrFE-CFE) polymer to study dielectric relaxation. The nanofibers reduced activation energy for space charge relaxation (Arrhenius) and α-relaxation (VFT), enhancing molecular mobility. Homogeneous BTO@TO_nfs dispersion improved local chain uniformity, narrowing α-relaxation time distribution (Dan *et al.* 2020). A triboelectric nanogenerator (TENG) was developed using PANI nanowires integrated with P(VDF-TrFE)/$BaTiO_3$ (BTO) electrospun fibers (PPVTB8/PY-TENG). It achieved 300 V, 77 µA, and 10 W m^{-2} power density, representing 500% voltage and 1300% current enhancement. The hybrid PPVTB8/NY-TENG-SCSPC also delivered 35.9 mF cm^{-2} capacitance and 4 µWh cm^{-2} energy density with >95% retention after 5000 cycles, suitable for self-powered wearable sensors (Mahanty *et al.* 2025).

Cross-linked solid polymer electrolytes (SPE-PIV) were fabricated by *in situ* polymerization using VC, VBIM-TFSI and octaMA-POSS within a POSS/ Polyvinylidene Fluoride (PVDF) matrix. The optimized polymer showed ionic conductivity of 9.02×10^{-4} S cm^{-1} (30 °C), Li^+ transference number 0.64, and 5.4 V electrochemical stability. The synergistic design improved interfacial contact, stability, and conductivity for high-performance solid state lithium-ion batteries (Hu *et al.* 2025). Electrospun PMMA–MXene–chitosan nanofibers were developed as multifunctional e-skin scaffolds. The composite achieved 13 MPa tensile strength, 0.38 GPa modulus, 28 W/m·K thermal conductivity, and >95% antimicrobial inhibition against *E. coli*, *S. aureus*, and *C. albicans*. High dielectric stability (tan δ < 0.05) and low impedance (1.38 kΩ) make it ideal for flexible bio-sensing and wound-healing devices (Gürbüz *et al.* 2025). A Li^+ ion-selective electrode (ISE) coated with PAH/PSS multilayers minimized gypsum scaling in lithium-rich brine. The sensor exhibited rapid response (<10 s), high Nernst slope (59.14 mV/dec), and strong ion selectivity. A brine-tailored data algorithm (bt-DDPA) enhanced accuracy by 46.06%, enabling stable continuous Li^+ monitoring (Xiang *et al.* 2024).

A chitosan/polyvinyl alcohol (CS/PVA)-based composite electrolyte integrated with ionic liquid and graphene oxide showed improved thermal and dielectric properties. The CS/PVA/IL-GO (4.0) film achieved maximum proton conductivity (1.76×10^{-3} S/m) and dielectric constant (9.55×10^4). Findings indicate suitability for high-efficiency energy storage devices (Yilmazoğlu *et al.* 2024). An electrospun cellulose acetate (CA) solid polymer electrolyte derived from bacterial cellulose showed enhanced porosity and conductivity (2.68×10^{-3} S/cm). The CA SPE demonstrated superior electrochemical stability (4.5 V) and improved lithium-ion mobility compared to bacterial cellulose-based electrolytes (Sabrina *et al.* 2024). Solvent-free polymer electrolytes were prepared by electrospinning and solution casting, showing distinct conductivity trends. Electrospun nanofibers exhibited higher ionic conductivity (0.062–0.172 mS/cm) and better dielectric behavior than cast films. These membranes demonstrate strong potential for Li-ion battery applications (Banitaba *et al.* 2022).

A PAN/PPy nanofiber-modified pencil graphite electrode was fabricated by electrospinning for detecting non-small cell lung cancer cells. Aptamer-functionalized sensor showed strong selectivity toward A549 cells and detection limit of 1.2×10^3 cells/mL. The label-free biosensor demonstrated high sensitivity and potential for clinical cancer diagnostics (Kivrak *et al.* 2020). PEO core–shell nanofibers including MWCNTs and SiO_2 nanoparticles were produced by electrospinning for solvent-free electrolytes. The optimized filler-loaded fibers showed enhanced ionic conductivity (0.21 mS/cm) and improved capacity retention (85%). These membranes exhibited Arrhenius-type behavior, suitable for Li-ion battery applications (Banitaba *et al.* 2020). Coaxially electrospun PAN/GO nanofiber mats were hot-pressed into flexible composite films with enhanced dielectric properties. Thermal reduction of GO to rGO and PAN structural reorientation yielded a dielectric constant up to 40 at 150 °C. The films maintained low loss and stability across a wide temperature range, ideal for high-temperature electronics (Su *et al.* 2020). Sol-gel-assisted electrospinning produced $NiFe_2O_4$/rGO fiber composites with temperature-dependent properties. Annealing at 600 °C yielded optimal electrochemical performance, achieving 650 F/g capacitance and low resistance (24.6 Ω). Enhanced crystallinity and charge transport made the composite ideal for supercapacitor applications (Gad *et al.* 2026). Electrospun carbon nanofibers incorporated with MnO_2 nanorods and rGO sheets enhanced capacitance and conductivity.

CNF/MnO_2 composites reached 271.4 F/g, while rGO/CNF achieved 251.5 F/g. An asymmetric device combining both electrodes showed a 2 V window with high energy density (34.4 W h/kg), confirming their efficiency for energy storage (Selvaraj *et al.* 2022).

The dielectric properties of PTh composites had not extensively investigated in previously stated investigations. The dielectric characteristics of PTh/PEO/rGO/TiO_2 nanofibers are insufficiently investigated in current literature. While studies have explored the electrical and dielectric characteristics of PTh-based nanocomposites, the specific mixture of PTh with PEO, reduced graphene oxide (rGO), and changing concentrations of nTiO_2 constitutes a novel study approach. This research is innovative in its analysis of the dielectric, electrochemical and structural characteristics of PTh/PEO/rGO/TiO_2 composite nanofibers created through electrospinning, emphasizing the improvement of electrical conductivity, supercapacitor efficacy and dielectric constants, by varying concentrations of TiO_2 and incorporation of rGO. Investigations have been conducted on the mechanisms of dielectric and electrical conductivity concerning frequency and temperature. The findings indicated that the interfacial method generated nanofibers due to the increased dielectric constant values. Supercapacitors can be utilized with these materials. This combination and the approach for enhancing the properties shows a significant improvement in energy storage, especially in improvement of improved supercapacitor electrode.

2. MATERIALS AND METHODOLOGY

2.1 Materials

All reagent-grade chemicals were employed as received. Thiophene and ferric chloride were utilized as the monomer and oxidizing agent, respectively. Hydrochloric acid, dimethylformamide (DMF), and polyethylene oxide with a molecular weight range of 1×10^5–8×10^6 g·mol^{-1} were used as processing additives. Reduced graphene oxide–titanium dioxide (rGO–TiO_2) hybrid nanomaterial served as the functional nanoparticulate reinforcement. All analytical-grade reagents were procured from Sigma-Aldrich (India).

2.2 Preparation of Polythiophene

Polythiophene was prepared by a chemical oxidative polymerization technique. Initially, thiophene monomer was dissolved in 50 mL of anhydrous chloroform and kept under continuous agitation in an ice bath at a temperature range of 0–5 °C to prevent premature polymerization. Ferric chloride was dissolved in 50 mL of chloroform in a separate beaker, maintaining a monomer-to-oxidant molar ratio of 1:4. The oxidant solution was introduced dropwise into the thiophene solution while maintaining continuous agitation. The polymerization reaction was permitted to continue for roughly 8 to 12 hours at ambient temperature. As the reaction advanced, the colour of the solution transitioned from pale yellow to deep black, signifying the formation of polythiophene chains. The precipitate was filtered and extensively washed multiple times with methanol, deionized water, and acetone to eliminate residual oxidant and unreacted monomer. The purified PTh powder was subsequently heated in a vacuum oven at 60 °C for 24 hours to provide a fine, conductive black powder.

2.3 Preparation of PTh/PEO/rGO/TiO_2 Nanofibers

To obtain a homogeneous PTh/PEO/rGO/TiO_2 composite, 0.005 g of rGO was first dispersed in 5 mL of DMF using ultrasonication for 2 h, followed by the addition of 0.05 g of PTh and continued mechanical stirring for another 2 h to enhance dispersion. For TiO_2-incorporated samples, different concentrations of TiO_2 nanoparticles were introduced into the PTh/rGO/DMF solution during ultrasonication, as listed in Table 1. Subsequently, 0.45 g of PEO was added to the mixture, which was then allowed to equilibrate overnight at room temperature to obtain a uniform spinning solution. The prepared polymer solution was taken in a plastic syringe and electrospun under an applied voltage of 11 kV, with the syringe tip acting as the anode and an aluminum foil–coated metallic collector as the cathode. A flow rate of 1 mL/h and a tip-to-collector distance of 10 cm were maintained throughout the process to fabricate PTh/PEO/rGO and PTh/PEO/rGO/TiO_2 nanofibrous mats (Fig. 1) for dielectric and electrochemical characterization.

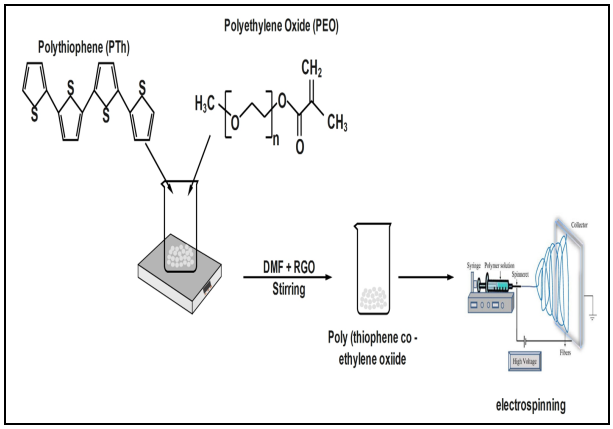


Fig. 1: Process for preparing PTh/PEO/rGO nanofiber

2.4 XRD

X-ray diffraction (XRD) patterns of the synthesized PNC was obtained using Panalytical Empyrean third generation instrument with Cu-Kα radiation (λ = 1.540 Å) at operating voltage of 30 kV.

Scanning was done with detector step size of 0.02° s^{-1} across angular range of 2θ from 10°- 80°.

Table 1. Composition of the composites

Sample	Contents
A	PTh/PEO + 0.005 g rGO
B	PTh/PEO + 0.005 g rGO + 0.0015 g TiO_2
C	PTh/PEO + 0.005 g rGO + 0.003 g TiO_2
D	PTh/PEO + 0.005 g rGO + 0.0045 g TiO_2
E	PTh/PEO+ 0.005 g rGO + 0.006 g TiO_2

2.5 Fourier Transform Infrared Spectroscopy

The FTIR spectrometer (Alpha II) from IRSpirit spectrometer (Shimadzu Corporation, Kyoto, Japan) equipped with diamond ATR system was utilized to obtain ATR-FTIR spectra at a resolution of 4 cm^{-1} within the spectral range 4000–500 cm^{-1} (Girimurugan *et al.* 2024).

2.6 Dielectric Characteristics

The nanofiber composite surfaces were covered (13 mm in diameter) with silver paste and dried at room temperature for 12 hours before taking measurements. After the specimen was connected to LCR analyzer, Ohmic contact was made between the electrodes (Zare *et al.* 2024). A Haioki IM-3533 LCR and Kelvin probe were used for the evaluation of dielectric properties at temperatures ranging from 30 °C to 100 °C.

2.7 Electrochemical Parameters

The electrochemical properties of the electrodes were examined utilizing a portable electrochemical station, specifically the CA00 multichannel potentiostat manufactured by Corretest (Ganvir *et al.* 2024).

3. RESULTS AND DISCUSSION

3.1 FT-IR Spectroscopy

The vibrational characteristics of the A–E nanofibers were analyzed using FT-IR spectroscopy to elucidate molecular structural differences between pure PTh and its composites incorporating various materials, including metal oxide nanoparticles. The FT-IR spectra of the A-E nanofibers are nearly indistinguishable, as shown in Fig. 2(a). The similarity in overall spectral profile and the absence of significant peak shifts or new functional groups, while the rGO-related O–H and C–O bands are present as weak, overlapping features arising from intrinsic rGO functional groups and interfacial interactions with the PTh/PEO matrix. The incorporation of rGO and TiO_2 nanoparticle into the PTh/PEO composite does not substantially alter the functional groups. The peak at 2925.45 cm^{-1} corresponds to the C-H stretching vibration PTh, whereas the peak at 1646.91 cm^{-1} is attributed to the C=C stretching vibration. The O-H stretching vibration of rGO was found at 3305.39 cm^{-1}, while the C-O stretching vibration was found at 1034.62 cm^{-1}. A prominent peak was observed at 1166.72 cm^{-1} corresponding to C-O-C stretching vibration.

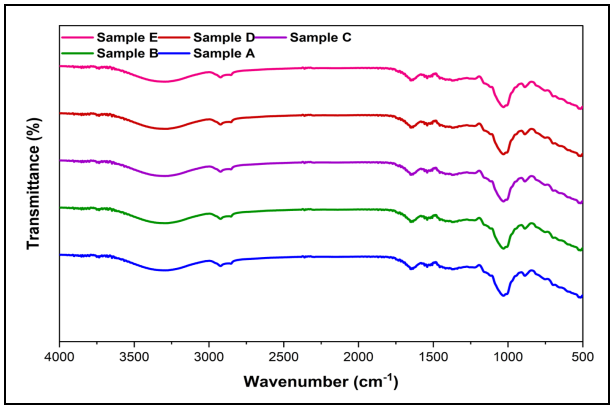


Fig. 2: FTIR spectra for the nanofiber (A-E) composites

3.2 Crystallization Behaviour

The XRD of nanofibers A–E are shown in Fig. 3. Two characteristics diffraction peaks were observed at 2θ = 22.8° and 17.4° (Huner, 2022). The overlapping peak at 2θ = 17.4° indicates that both PTh and PEO contribute to this diffraction plane, confirming their good compatibility within the composite system. The peak at 2θ = 22.8° becomes progressively sharper with increasing TiO_2 nanoparticles concentration, suggesting enhanced crystallinity of the composite nanofibers. A similar trend was reported in a previous study, where PVDF nanofiber mats incorporated TiO_2–Fe_3O_4–GO hybrid nanoparticles to improve piezoelectric and electromagnetic performance. Specifically, the β-phase content of PVDF increased by ~79% as determined by FTIR analysis and 15% by XRD analysis at 2 wt% filler loading, leading to enhanced polarization and piezoelectric response (Haji *et al.* 2022).

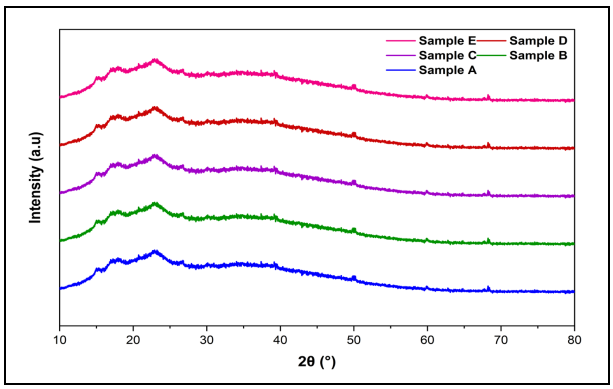


Fig. 3: XRD patterns of the nanofiber (A-E) composites

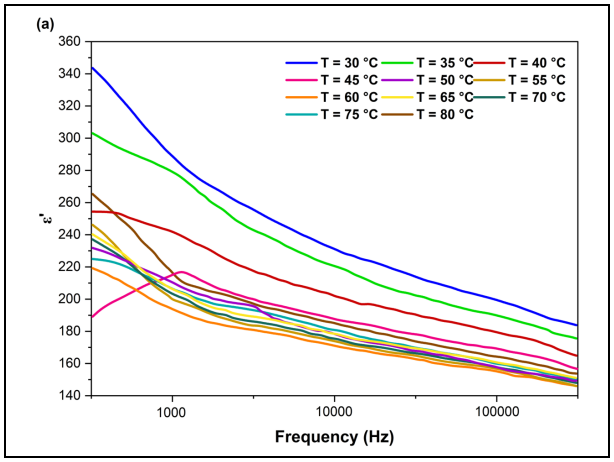
3.3 Dielectric Properties

Measuring dielectric characteristics is an effective method to obtain information about the charge carriers in composites when subjected to electric fields. Imposing an electric field on a dielectric induces polarization, wherein charges migrate toward the positive and negative electrodes.

The complex dielectric permittivity (Ɛ), a frequency-dependent parameter is defined as follows.

$$\varepsilon = \varepsilon' - j\varepsilon'' \qquad \ldots (1)$$

The real and imaginary components of complex permittivity denoted as ε′ and ε″, respectively, signify the dissipated and energy stored during each cycle. Except for C, the dielectric constant reduced with increasing frequency, attaining its minimum at approximately 100000 Hz across all samples and temperatures. Free dipoles exposed to external fields exhibit oscillations that correlate with the dielectric constant. The dipole moment aligns with the applied fields, while the dielectric constant (ε) exhibits elevated values at reduced frequencies (Zahari *et al.* 2025). A greater dielectric constant results from significant space charge polarization, which transpires when charges a mass at interfaces. The dipoles lag behind the applied field at elevated frequencies due to their inability to rotate rapidly to match the periodic polarity fluctuations. A variety of processes contribute to the elevation of the average dielectric constant at lower frequencies and its reduction at higher frequencies. While conducting polymers are recognized for the absence of dipole moments, charge carriers may demonstrate dipole behavior under the influence of electric fields (Elmessiry *et al.* 2021). The increase in the dielectric constants of these polymers with temperature indicates that their effective electric dipoles exhibit enhanced mobility. Doping PTh/PEO and rGO with TiO_2 nanoparticles increases the dielectric constant. Fig. 4 illustrates the variation of dielectric constant (ε") with frequency across different temperatures.



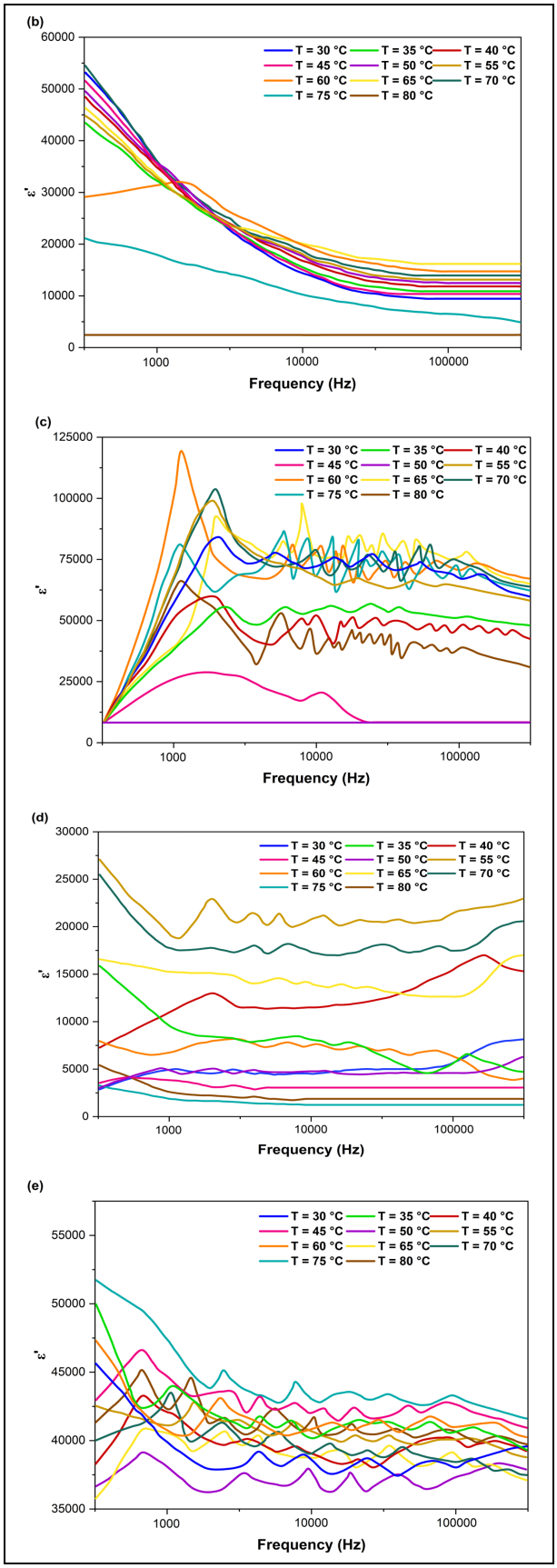


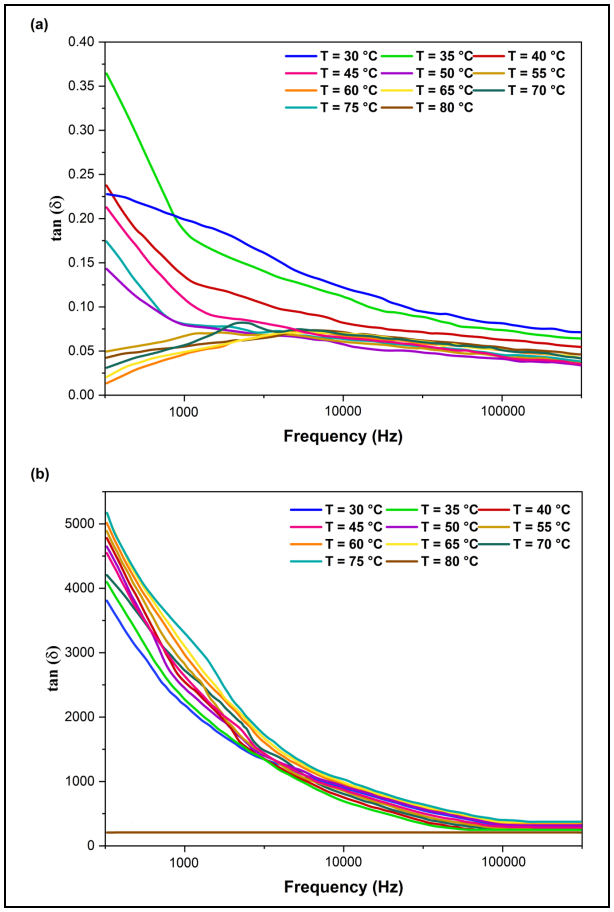
Fig. 4: Frequency-dependent dielectric constant of (A-E) nanofibers at various temperatures

Fig. 5 illustrates variation of dielectric loss (ε'') with frequency across various temperatures. When specimens function as capacitors, dielectric loss refers to the energy dissipation occurring within the samples. The experimental results show that dielectric loss escalates with frequency reduction (f < 10 kHz). The dielectric loss values decline significantly and remain stable as the frequencies increase (Z>10 kHz), and this pattern persists. This indicates that the samples serve as effective polymer conductors at elevated frequencies. Reduced graphene oxide enhanced the dielectric characteristics of the PTh/PEO/TiO_2 composite. Furthermore, TiO_2 nanoparticles can function as electrodes within the sample for nanoscale capacitors, hence enhancing capacitance and reducing energy loss within the capacitor.

3.4 Conduction Mechanism and AC Conductivity

The charge conduction mechanism can be elucidated by examining the AC electrical conductivity of disordered composites, thereby allowing for the calculation of AC conductivity σAC(ω) by the following equation (2) (Ajila *et al.* 2024).

$$\sigma'(\omega)_{AC} = 2\pi f \varepsilon_0 \varepsilon'' \quad \ldots (2)$$



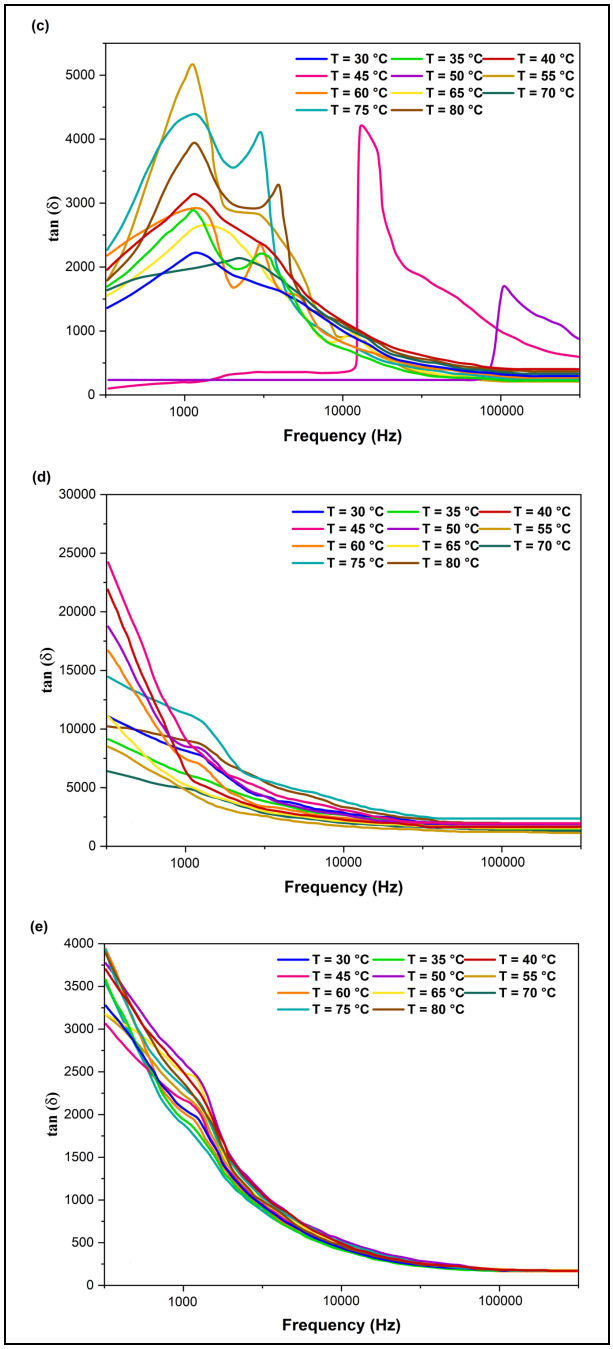
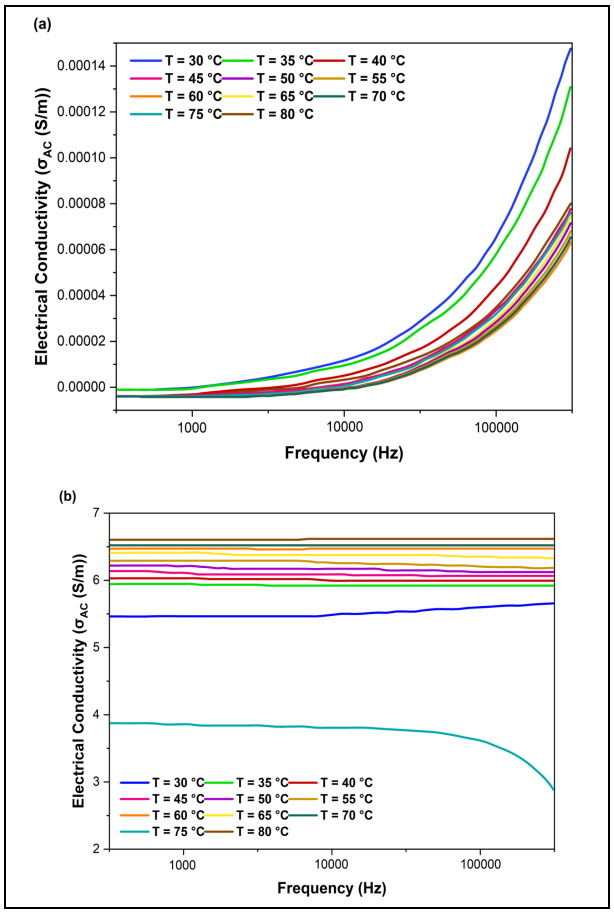


Fig. 5: Frequency-dependent dielectric loss of (A-E) nanofibers at various temperatures

In this context, the free-space permittivity (ϵ_0), dielectric loss (ϵ''), and applied alternating field frequency (f) are all variables. In previous study, the electrospun material showed strong Polyaniline (PAN)–Graphene oxide (GO) interaction by hydrogen bonding, improving thermal stability. Dielectric studies revealed high permittivity (86.4) and conductivity (34.9 × 10^{-6} S/m), making it promising for flexible electronic devices (Almafie *et al.* 2022). Fig. 6 illustrates the AC conductivity σAC(ω) for both pure PTh and doped composites across different temperatures. The results for

AC conductivity indicated that σ-AC remains frequency-independent at lower frequencies (about 1000 to 10000 Hz) but exhibits a significant increase at higher frequencies (around 100000 Hz). The frequency-independent region at low frequency corresponds to DC conductivity, while the dispersive region at higher frequency is attributed to transport of charge carriers. Doping PTh/PEO with rGO and nanoTiO_2 significantly increases the AC conductivity by several orders of magnitude due to the properties of nTiO_2. Generally, composite systems cannot conduct electricity without employing some form of quantum mechanical tunneling or hopping. The AC conductivity graph illustrates that conductivity escalates with increasing temperature. According to Jonscher's universal power law, the AC conductivity can be expressed as $\sigma AC(\omega) = \sigma DC + A\omega s$, where the frequency exponent 's' provides insight into the dominant conduction mechanism. For correlated barrier hopping (CBH)-type conduction, 's' decreases with increasing temperature due to enhanced charge carrier hopping over potential barriers, whereas overlapping large polaron tunneling (OLPT) conduction is associated with weak temperature dependence of 's' caused by overlapping polaron potential wells.



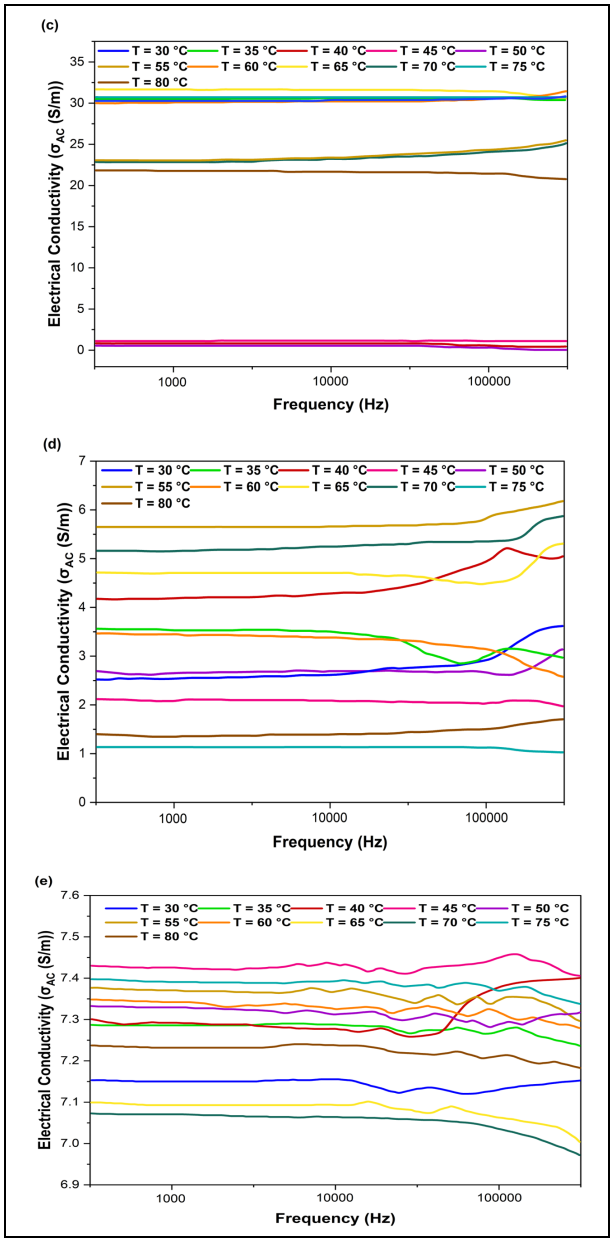


Fig. 6: Electrically conductive property (σAC) of (A-E) nanofibers at various temperatures as an indicator of frequency

Samples A, D, and E demonstrate an increasing conductivity value with increasing temperature. This behavior characterized by an increase in σAC with temperature and dispersive conductivity at higher frequencies is consistent with the CBH mechanism for pure PTh and rGO/TiO_2-doped PTh nanofibers. In contrast, samples B and C exhibit conductivity behavior consistent with the OLPT mechanism, where strong long-range Coulomb interactions promote the overlap of potential wells between neighboring localized sites.

3.5 Electrochemical Measurements

Specimens A–E were employed as supercapacitor electrodes. A binder slurry (1 mL) consisting of alcohol, isopropyl alcohol, and Nafion (0.1:5:5, v/v), diluted with deionized water was used to attach a 1 cm × 1.5 cm nickel foam current collector to a 1 cm × 1 cm nanofiber. A three-electrode system was used with the composite-coated Ni foam as the working electrode, Hg/HgO as the reference electrode, and a platinum wire used as the counter electrode.

The electrochemical volume of various supercapacitor electrode substances were examined on 1 M KOH electrolyte, employing electrochemical impedance spectroscopy, galvanostatic charge-discharge (GCD), and cyclic voltammetry (CV) techniques. The working electrodes used were A–E on NF, the reference electrode was Hg/HgO and counter electrode was a platinum wire.

The CV curves of nanofibers (A-E) exhibit pseudocapacitive behavior at sweep rate of 50 mV/s, displaying peak currents on both the anode and cathode. A polythiophene-based system that exhibits polymer-like conductivity incorporates a charge storage mechanism. This approach employs surface capacitive charge, facilitated by a redox transformation in the ionic diffusion process, due to the double layer and faradaic charge. A scan rate of 50 mV/s was selected as a representative condition to enable a direct and consistent comparison of the electrochemical behavior of all nanofiber samples (A–E). Fig. 7(a) illustrates that the magnitude of the CV curves increases with the scan rate, where the redox peaks remain consistent in structure. Reducing the interval time for electrochemical testing and increasing the sweep rate demonstrated remarkable high-rate capacity and reversibility.

To further evaluate the rate-dependent electrochemical kinetics and capacitive performance, sample E was subsequently examined over a broader scan rate range of 5–80 mV/s. Fig. 7(b) illustrates the comprehensive cyclic voltammetry of E on the nickel foam within a potential range of 0.2 to 0.8 V, at scan rates varying from 5 to 80 mV/s. The anodic peaks shift to lower potentials while the cathodic peaks shift to higher potentials with increasing scan speeds. The absence of variation in peak potentials with increased scan rate indicates the influence of electrochemical polarization and kinetic limitations of PTh. The specific capacitance (Cs) of E was calculated from the CV curves using the subsequent equation (3) (Khawale *et al.* 2024).

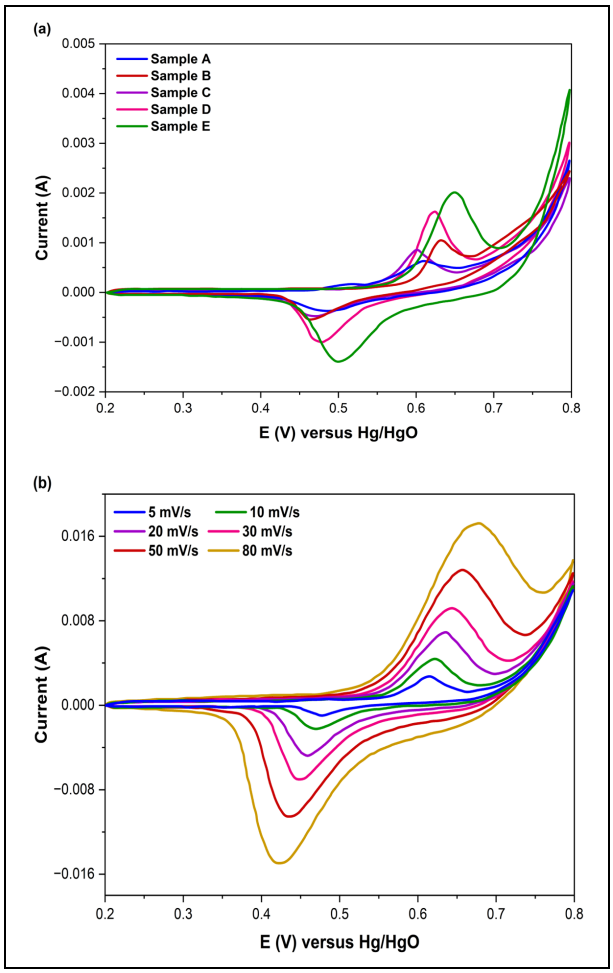
$$C_A = \frac{\int IdV}{A\nu\Delta V} \quad \ldots (3)$$

The calculated areal capacitances for the E electrode material on NF scan rates of 5, 10, 20, 30, 50, and 80 mV s^{-1} are 408.35, 367.14, 291.79, 260.53, 238.06 and 182.48 mF cm^{-3}, respectively.

A range of 0.2 – 0.8 V is employed to obtain GCD curves to analyze the behavior of A to E during charging and discharging on NF electrodes. Fig. 7(c) illustrates the GCD curves for sets A–E on NF electrodes at a current density of 2 mA·cm^{-2}. Fig. 7(d) illustrates GCD curves of E at the NF electrode on various current densities 1.2, 1.8, 2.4, 3.0, then 3.6 mA cm^{-2}. To provide a fair comparison among all prepared electrodes, GCD curves of samples A–E were initially recorded at a fixed current density of 2 mA·cm^{-2}. Furthermore, the optimized electrode (E) was subjected to GCD analysis at different current densities to evaluate its rate capability.

$$C_A = \frac{I\Delta t}{A\Delta V} \quad \ldots (4)$$

The charge-discharge current (I), discharge duration (Δt), and electrode material area (A) are all specified in square centimeters. ΔV denotes the potential window, represented as V.



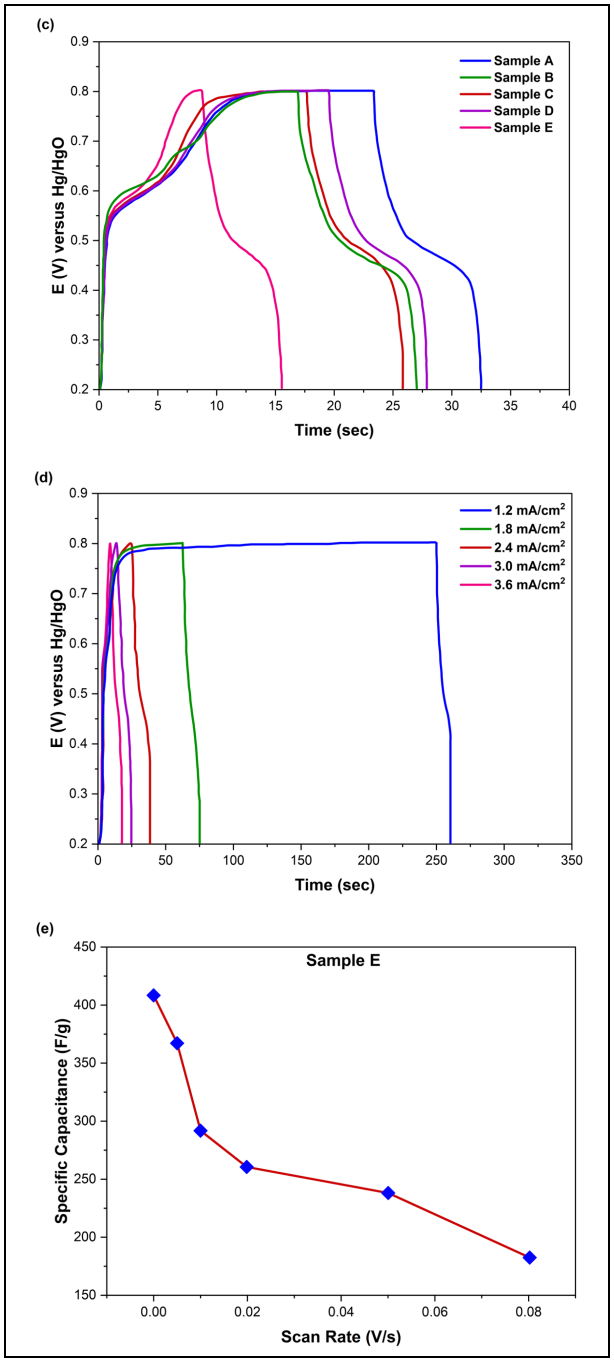


Fig.7: Performance of (A-E) nanofibers in 1 M KOH (a) A to E at NF CV curves (b) E on NF CV curves at different scan rates (c) A to E on NF GCD curves at current density (d) E on NF supercapacitor and (e) relationship among areal capacitance at various scan rates

Charge-discharge indicates that the areal capacitance of E was 408.35, 367.14, 291.79, 260.53, 238.06 and 182.48 mF·cm^{-2}, corresponding to 1.2, 1.8, 2.4, 3.0, and 3.6 mA·cm^{-2}. Fig. 7(e) illustrates that specific capacitance values inversely related to varying scan rates in 1 M KOH, indicating a decline in specific capacitance as scan rates increases.

The effect of capacitive contribution can be subjectively assessed by examining the correlation between peak current (i) and scan rate (v), as given in Equation 5.

$$i = av^b \quad \ldots (5)$$

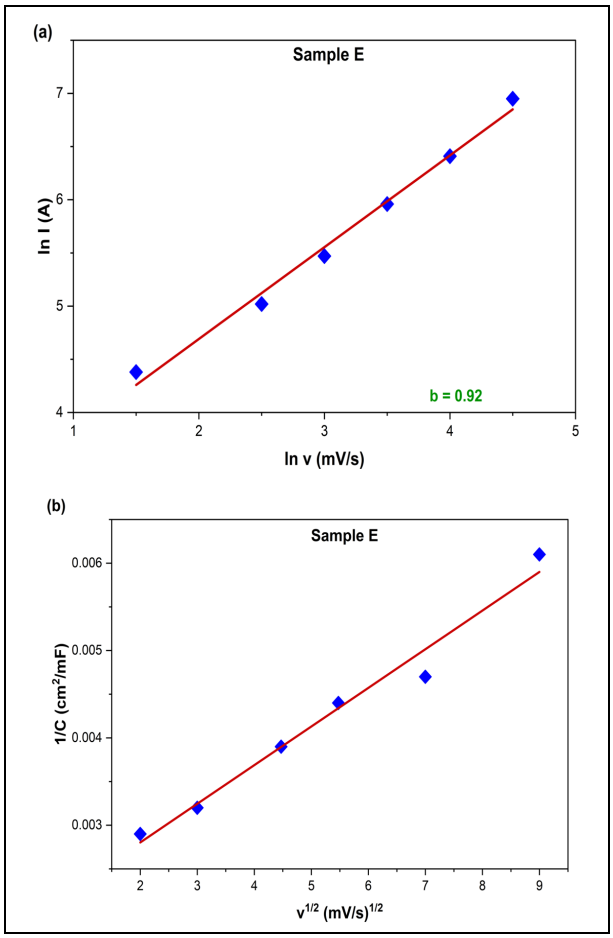
The parameter b quantifies the kinetics of charge storage. A b value of 0.5 shows a diffusion-controlled process, value of 1 denotes capacitive behavior. Fig. 8(a) illustrates that for scan velocities of 5, 10, 20, 30, 50, and 80 mV/s, the value of b for E nanofiber is 0.92.

Assuming ion diffusion follows a semi-infinite diffusion model, a linear relationship is expected between the predicted areal capacitances and square root of scan rates

$$C^{-1} = \text{constant } v^{-1/2} + C_T^{-1} \quad \ldots (6)$$

Equation (7) indicates that the calculated areal capacitances in Fig. 8(c) exhibit a linear relationship with inverse of square root of scan rates.

$$C = \text{constant } v^{-1/2} + C_{EDL} \quad \ldots (7)$$



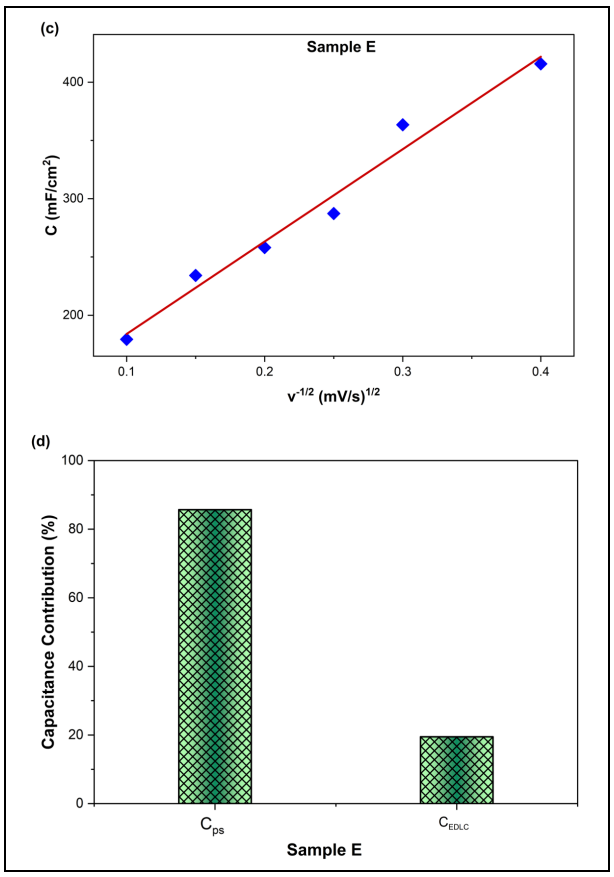


Fig. 8: (a) Reciprocal of areal capacitance *vs.* square root of scan rate, (b) Plot of reciprocal of areal capacitance *vs.* square root of scan rate, (c) Plot of areal capacitance *vs.* reciprocal of square root of scan rate and (d) Bar plot of percentage of capacitance contribution evaluated of E on NF

By subtracting highest capacitance from peak electron double layer capacitance, one can derive the highest pseudo-capacitance. Consequently, the capacitance contribution can be determined utilizing the subsequent equations. Fig. 8(d) presents a comparative plot of the two capacities in sample E.

$$C_{EDL}\% = \frac{C_{EDL}}{C_T} \times 100 \quad \ldots (8)$$

$$C_{ps}\% = \frac{C_{ps}}{C_T} \times 100 \quad \ldots (9)$$

Electrochemical impedance spectroscopy can be employed to assess the electrical properties of electrode for supercapacitor uses (Sarac *et al.* 2024). Fig. 9(a) illustrates Nyquist plot on NF for A - E, with an alternating current voltage amplitude of 10 mV, across the frequency range of 1.0−300 kHz. By utilizing the semicircle diameter, the charge transfer resistance (R_{ct}) and the solution resistance (R_s) were ascertained through the calculation of the high-frequency intercept on the real axis (Z-′). E on NF exhibited a resistance rating of 0.992 Ω, indicating low resistance. Table 2 illustrates the values of R_s and R_{ct} for individual specimen. The low R_{ct} for E on NF indicates a compact semicircle in the high-frequency area. E exhibits a recorded R_{ct} value of 0.13 Ω on NF.

Table 2. R_{ct} and R_s values for A−E on NF using Nyquist plot

Sample	R_{Ct} (Ω)	R_S(Ω)
A	0.45	1.9
B	0.23	1.7
C	0.23	1.6
D	0.23	1.5
E	0.13	0.992

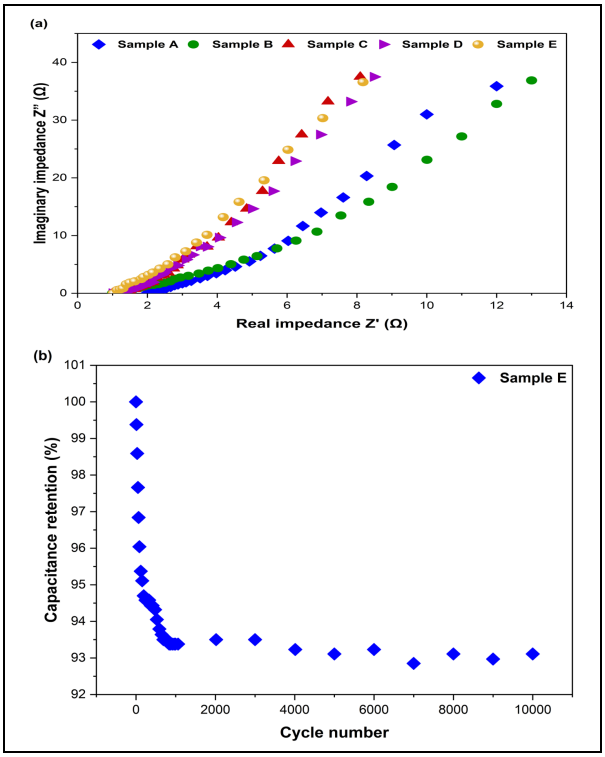


Fig. 9: (a) EIS-tested Nyquist plots of (A-E) nanofibers on NF as supercapacitor x-axis 0 to 3 ohms (b) Long-term (more than 10,000 cycles) cyclic stability of E on NF 3 mA

Assessing the cyclic stability of supercapacitor electrode materials is crucial for evaluating its performance rate. Fig. 9(b) illustrates that the pseudocapacitance exhibited cyclic stability within potential range of 0.2 − 0.8V during GCD for 10,000 cycles at a constant current density of 3.6 $mA \cdot cm^{-2}$. Following about 10,000 cycles, the capacity preservation of E attained 93.06%. The findings indicate that E on the NF electrode exhibits exceptional long-term cycle stability, which is crucial for supercapacitor applications. In prior studies, electrospun PEO-based fibrous electrolytes were doped with CuO, NiO, and Co_3O_4

nanoparticles to enhance ASSLB performance. In Li|$LiCoO_2$ cells, discharge capacity increased from 68 to 120 mAh g^{-1} at 0.5 C for 100 cycles, proving superior electrochemical effect of CuO (Banitaba *et al.* 2021).

4. CONCLUSION

Nanofibers (PTh/PEO/rGO/TiO_2) with varying TiO_2 nanoparticle content were successfully synthesized *via* electrospinning. XRD analysis confirmed the predominantly amorphous nature of the nanocomposite structure. The incorporation of TiO_2 nanoparticles improved interfacial polarization, resulting in an enhanced dielectric constant and reduced dielectric loss. The presence of rGO within the PTh/PEO matrix further improved alternating current conductivity, particularly for samples D and E, indicating the effectiveness of interfacial engineering in tuning electrical properties. These enhanced dielectric and conductive characteristics directly contributed to improved electrochemical performance when the nanofibers were employed as supercapacitor electrodes. Among all samples, composite E deposited on nickel foam exhibited superior electrochemical behavior, delivering an areal capacitance of 408.35 mF cm^{-2} and retaining 93.06% capacitance after 10,000 charge–discharge cycles. The low series resistance (0.992 Ω) further confirms efficient charge transport and electrode stability. Overall, the systematic integration of rGO and TiO_2 nanoparticles within the PTh/PEO nanofiber matrix demonstrates an effective strategy for simultaneously enhancing dielectric and supercapacitor performance, highlighting the potential of PTh/PEO/rGO/TiO_2 nanofibers for advanced solid-state energy storage applications.

FUNDING

This research received no specific grant from any funding agency in the public, commercial, or not-for-profit sectors.

CONFLICTS OF INTEREST

The authors declare that there is no conflict of interest.

COPYRIGHT

This article is an open-access article distributed under the terms and conditions of the Creative Commons Attribution (CC BY) license (http://creativecommons.org/licenses/by/4.0/).



REFERENCES

Ajila, F., Manokaran, S., Ramaswamy, K., Thiyagarajan, D., Praveen, P., Shaik, M. A., Dillibabu, S. P., Kiran, U. K. and Selvaraju, M., Prediction of Nanofluid Thermal Conductivity and Viscosity with Machine Learning and Molecular Dynamics, *Therm. Sci.,* 28(1), 717–729(2024). https://doi.org/10.2298/TSCI230312005A

Almafie, M. R., Marlina, L., Riyanto, R., Jauhari, J., Nawawi, Z. and Sriyanti, I., Dielectric Properties and Flexibility of Polyacrylonitrile/Graphene Oxide Composite Nanofibers, 7(37), 33087–33096(2022). https://doi.org/10.1021/acsomega.2c03144

Banitaba, S. N., Semnani, D., Heydari-Soureshjani, E., Arifeen, W. U., Ko, T. J., Rezaei, B., Ensafi, A. A., Latifi, M., Mostafavi, E. and Kaushik, A., Fabrication and performance evaluation of CuO, NiO, and Co_3O_4-embedded electrospun electrolytes: Suitable for lithium polymer solvent-free batteries, *J. Alloys Comp.,* 924, 166482(2022). https://doi.org/10.1016/j.jallcom.2022.166482

Banitaba, S. N., Semnani, D., Heydari-Soureshjani, E., Rezaei, B. and Ensafi, A. A., Electrospun core-shell nanofibers based on polyethylene oxide reinforced by multiwalled carbon nanotube and silicon dioxide nanofillers: A novel and effective solvent-free electrolyte for lithium-ion batteries, *Int. J. Energy Res.,* 44(8), 7000–7014(2021). https://doi.org/10.1002/er.5475

Banitaba, S. N., Semnani, D., Karimi, M., Heydari-Soureshjani, E., Rezaei, B., and Ensafi, A. A. (2021). A comparative analysis on the morphology and electrochemical performances of solution-casted and electrospun PEO-based electrolytes: The effect of fiber diameter and surface density, *Electrochimica Acta,* 368, 137339(2020). https://doi.org/10.1016/j.electacta.2020.137339

Dan, Z., Jiang, J., Zhang, X., Qian, J., Shen, Z., Nan, C. and Shen, Y., Interfacial effects of $BaTiO_3$@TiO_2 nanofibers on dielectric relaxation processes of P(VDF-TrFE-CFE) nanocomposites, *Ceram. Int.,* 46(1), 1119–1123(2020). https://doi.org/10.1016/j.ceramint.2019.09.080

Elmessiry, K. S., ElAassar, M. R., Nassr, A. B. A. A., Kenawy, E. R., Moharam, B. E. and Ali, N., Free-Standing Working Electrodes for Supercapacitors Based on Composite Polymer Nanofibers and Functionalized with Graphene Oxide, *J. Elec. Mater.*, 50(10), 5599–5611(2021). https://doi.org/10.1007/s11664-021-09120-2

Gad, S., Rafea, M. A., Fawal, G. E., Zaki, M. E. A., Elsharkawy, S. G. and Khalil, H. F., Temperature dependent crystallinity, DFT calculations and electrochemical behavior of NiFe2O4/reduced graphene oxide fiber electrodes for high-performance supercapacitors, *Mater. Res. Bulletin*, 195, 113845(2026). https://doi.org/10.1016/j.materresbull.2025.113845

Ganvir, H. V., Kumar, S., Kumar, R., Haldar, B., Satishkumar, S., Verma, R., Dolas, D. R., Arun, V., Jadhav, V. D. and Selvaraju, M., Monitoring Atomic Layer Deposition by Potentiodynamic Electrochemical Impedance Spectroscopy of Multielement Adlayers, *J. New Mater. Electrochem. Syst.,* 27(3), 172–181(2024). https://doi.org/10.14447/jnmes.v27i3.a02

Girimurugan, R., Selvaraju, M., Shine, S. and Khaled, J. M., Investigation on Polypyrrole-Induced Modification of Aspergillus flavus: Evaluation of Biocompatibility and Electrochemical Properties, *J. New Mater. Eectrochem. Syst.,* 27(3), 190–198(2024). https://doi.org/10.14447/jnmes.v27i3.a04

Gorgani, S., Kermani, F., Sadeghzadeh, K., Vojdani, A., Hooshmand, S., Foroughi, K., Azari, Z., Hosseini, S. A., Mollazadeh, S., Bideskan, A. E. and Nazarnezhad, S., Electrospun nanofibrous scaffolds reinforced with therapeutic lithium/manganese-doped calcium phosphates: Advancing skin cancer therapy through apoptosis induction, *Colloids Surf. B Biointer*., 245, 114348(2025). https://doi.org/10.1016/j.colsurfb.2024.114348

Gürbüz, B., Çıftçı, F., Özarslan, A. C. and Akyuz Yilmaz, B., MXene-modified PMMA/chitosan composite e-skin scaffold: Bioelectronic and antibacterial assessment, *Int. J. Bio. Macromol*., 319, 145388(2025). https://doi.org/10.1016/j.ijbiomac.2025.145388

Haji, A. M., Abdollahi, H. and Samadi, A., PVDF nanofibers containing GO-supported TiO_2–Fe_3O_4 nanoparticle-nanosheets: piezoelectric and electromagnetic sensitivity, *J. Mater. Sci. Mater. Electron.,* 33(8), 5970–5982. https://doi.org/10.1007/s10854-022-07777-x

Hong, J., Wang, N., Shi, H., Pang, Y., Ou, H., Wang, Y., Fan, B., Peng, Q. and Yuan, H., Metal-organic framework incorporated PEO-based flexible polymer electrolyte for advanced all-solid-state sodium-ion batteries, *J. Mater. Sci. Technol*., 255, 56–64(2026). https://doi.org/10.1016/j.jmst.2025.07.048

Hu, X., Ma, J., Gao, C., Ma, X., Wang, L. and Chen, F., In-situ polymerized high-ionic conductivity vinyl-based copolymer in electrospinning membrane for lithium-ion batteries, *Colloids Surf. A Physiochem. Eng. Aspects*, 719, 137016(2025). https://doi.org/10.1016/j.colsurfa.2025.137016

Huner, K., Fabrication of Water-Soluble Polythiophene/Poly (sulfonic acid diphenyl aniline)/Polyethylene Oxide Electrospun Nanofibers and Their Antioxidant Activities, *Chem. Select*, 7(36), 03166(2022). https://doi.org/10.1002/slct.202203166

Khawale, V. R., Mayank, Ranade, R., Satishkumar, S., Haldar, B., Deepa, B., Saminathan, R., Veeramanikandan, P., Packirisamy, A. S. B. and Selvaraju, M., Study on Electrochemical Stability and Charge Transfer Efficiency for the Development of High-Performance Supercapacitors Using Iron Oxide (Fe_2O_3) Nanorods, *J. New Mater. Electrochem. Syst*., 27(3), 163–171(2024). https://doi.org/10.14447/jnmes.v27i3.a01

Kivrak, E., İNce Yardimci, A., İLhan, R., Ballar Kirmizibayrak, P. B., Yilmaz, S. and Kara, P., Aptamer-based electrochemical biosensing strategy toward human non-small cell lung cancer using polyacrylonitrile/polypyrrole nanofibers, *Analyt. Bioanalyt. Chem*., 412(28), 7851–7860(2020). https://doi.org/10.1007/s00216-020-02916-x

Li, F., Song, H., Yu, W., Ma, Q., Dong, X., Wang, J. and Liu, G., Electrospun TiO_2//SnO_2 Janus nanofibers and its application in ethanol sensing, *Mater. Lett*., 262, 127070(2020). https://doi.org/10.1016/j.matlet.2019.127070

Mahanty, B., Ghosh, S. K., Malavekar, D. B., Kim, J. H., and Lee, D. W., PANI nanowire-decorated electrospun composite nanofibers for advanced triboelectric Nanogenerators and rectifier-free self-charging supercapacitors, *Chem. Eng. J*., 519, 165418(2025). https://doi.org/10.1016/j.cej.2025.165418

Sabrina, Q., Sudaryanto, S., Majid, N., Sugawara, A., Hsu, Y. I., Yudiantí, R. and Uyama, H., Electrospinning of Bacterial Cellulose Modified with Acetyl Groups for Polymer Electrolyte Li-Ion Batteries, *J. Electron. Mater*., 53(4), 2062–2075(2024). https://doi.org/10.1007/s11664-024-10958-5

Sarac, B., Gürbüz, R., Soprunyuk, V., Yüce, E., Rezvan, A., Schranz, W., Eckert, J., Özcan, A. and Saraç, A. S., Chitosan-containing electrospun poly (ethylene oxide)-polybutadiene-CNT fibers, *Polym. Adv. Tchnol.,* 35(4), 6403(2024). https://doi.org/10.1002/pat.6403

Selvaraj, A. R., Raja, I. S., Chinnadurai, D., Rajendiran, R., Cho, I., Han, D. W. and Prabakar, K., Electrospun One-Dimensional (1D) Pseudocapacitive nanorods embedded carbon nanofiber as positrode and graphene wrapped carbon nanofiber as negatrode for enhanced electrochemical energy storage, J. Energy Storage, 46, 103731(2022). https://doi.org/10.1016/j.est.2021.103731

Su, Y., Zhang, W., Lan, J., Sui, G., Zhang, H. and Yang, X., Flexible Reduced Graphene Oxide/Polyacrylonitrile Dielectric Nanocomposite Films for High-Temperature Electronics Applications, *ACS Appli. Nano Mater.,* 3(7), 7005–7015(2020). https://doi.org/10.1021/acsanm.0c01328

Thomas, M. and Rajiv, S., Grafted PEO polymeric ionic liquid nanocomposite electrospun membrane for efficient and stable dye sensitized solar cell, *Electrochimica Acta,* 341, 136040(2020). https://doi.org/10.1016/j.electacta.2020.136040

Wang, H., Nie, G., Wang, Z., Cui, S., Li, H., Dang, L., Pu, Z., Liu, X., Fu, A., Guo, Y. G. and Li, H., Carbon nanofibers with uniformly embedded silicon nanoparticles as self-standing anode for high-performance lithium-ion battery, *Colloids Surf. A Physicochem. Eng. Aspects*, 671, 131653(2023a). https://doi.org/10.1016/j.colsurfa.2023.131653

Wang, L., Dong, L., Wang, Z., Shangguan, E., Li, J., Li, L., Gao, S. and Deng, N., Engineering 3D Interpenetrated ZIF-8 Network in Poly(ethylene oxide) Composite Electrolyte for Fast Lithium-Ion Conduction and Effective Lithium-Dendrite Inhibition, *ACS Sustain. Chem. Eng*., 11(25), 9337–9348(2023b). https://doi.org/10.1021/acssuschemeng.3c00626

Xiang, W., Wang, X., Zhang, M., Aderibigbe, A. D., Wang, F., Zhao, Z., Fan, Y., Huey, B. D., McCutcheon, J. R. and Li, B., Continuous Monitoring of Lithium Ions in Lithium-Rich Brine Using Ion Selective Electrode Sensors Modified with Polyelectrolyte Multilayers of Poly(allylamine hydrochloride)/Poly(sodium 4-styrenesulfonate), *Environ. Sci. Technol*., 58(50), 22442–22455(2024). https://doi.org/10.1021/acs.est.4c07155

Yilmazoğlu, M., Okkay, H., Abaci, U. and Coban, O., Proton conductivity and dielectric studies on chitosan/polyvinyl alcohol blend electrolytes: Synergistic improvements with ionic liquid and graphene oxide, *Int. J. Bio. Macromol*., 279, 135502(2024). https://doi.org/10.1016/j.ijbiomac.2024.135502

Zahari, A. S., Mazwir, M. H., Misnon, I. I., Zulkifli, F. H., Hj Jumali, M. H. H. and Jamil, N. H. J., Piezoelectric and Dielectric Properties of Electrospun Polyvinylidene Fluoride (PVDF) Blended with Cellulose Nanocrystals (CNCs), *Macromol. Symposia,* 414(1), 2300248(2025). https://doi.org/10.1002/masy.202300248

Zare, M., Jamilpanah, L., Barough, V., Sadeghi, A., Ghanaatshoar, M. and Mohseni, M., Role of electrospun fibers coated on magnetoimpedance effect of Co-based ribbons, *Appl. Phys. A,* 130(2), 90(2024). https://doi.org/10.1007/s00339-023-07236-2